

# Mitigation of sensor inhomogeneities to speed up diamond-based wide-field magnetic imaging

Zeeshawn Kazi,<sup>1,\*</sup> Isaac M. Shelby,<sup>1</sup> Hideyuki Watanabe,<sup>2</sup> Kohei M. Itoh,<sup>3,4</sup>  
Vaithiyalingam Shutthanandan,<sup>5</sup> Paul A. Wiggins,<sup>1,6</sup> and Kai-Mei C. Fu<sup>1,7</sup>

<sup>1</sup>*University of Washington, Physics Department, Seattle, WA, 98105, USA*

<sup>2</sup>*Nanoelectronics Research Institute, National Institute of Advanced Industrial Science and Technology, Tsukuba Central 2, 1-1-1 Umezono, Tsukuba, Ibaraki 305-8568, Japan*

<sup>3</sup>*Spintronics Research Center, Keio University, 3-14-1 Hiyoshi, Kohoku-ku, Yokohama 223-8522, Japan*

<sup>4</sup>*School of Fundamental Science and Technology, Keio University, 3-14-1 Hiyoshi, Kohoku-ku, Yokohama 223-8522, Japan*

<sup>5</sup>*Environmental and Molecular Sciences Laboratory, Pacific Northwest National Laboratory, Richland, WA, USA*

<sup>6</sup>*University of Washington, Bioengineering Department, Seattle, WA, 98105, USA*

<sup>7</sup>*University of Washington, Electrical and Computer Engineering Department, Seattle, WA, 98105, USA*

Wide-field magnetometry can be realized by imaging the optically-detected magnetic resonance of diamond nitrogen vacancy (NV) center ensembles. However, sensor inhomogeneities significantly limit the magnetic field sensitivity of these measurements. We report a technique for mitigating NV ensemble inhomogeneities to speed up absolute magnetic imaging which uses a double-double quantum (DDQ) driving scheme. DDQ difference imaging employs four-tone radio frequency pulses to suppress inhomogeneity-induced variations of the resonant response, enabling a linear mapping between the magnetic field projection onto the NV ensemble symmetry axis and changes in the emitted NV photoluminescence intensity. This simple and robust technique expands the application space of diamond NV centers by extending existing NV absolute magnetic sensing techniques to rapid, wide-field imaging.

## INTRODUCTION

The success of the nitrogen-vacancy (NV) center in diamond as a magnetic field sensor is due to the powerful combination of a long spin-coherence time, the ability to perform optically-detected magnetic resonance (ODMR) at room temperature, and a solid-state host environment which facilitates sample-sensor integration [1–4]. One exciting emerging application is magnetic field imaging using a thin layer of NV centers near the surface of a diamond substrate [5–9]. In this NV ensemble imaging system, it is critical that the inhomogeneities across the sensor surface are eliminated in order to reach the noise floor given by the single-pixel sensor resonance curve. To this end, the NV community has demonstrated many sensor growth and fabrication methods that increase NV density and sensor homogeneity [10–15], as well as quantum control methods that suppress external field dependence and increase ensemble coherence [16–19]. In this paper, we expand on these techniques to present a quantum control method compatible with magnetic field imaging with high temporal resolution. Our method, double-double quantum (DDQ) driving, mitigates noise caused by variations of the sensor resonance curve.

In NV ensemble ODMR, magnetic fields can be imaged by characterizing the photoluminescence of optically-excited NV centers while rotating the NV spin states with radio frequency (RF) pulses [Fig. 1]. The resonant radio

frequency depends on magnetic field due to the Zeeman splitting of two NV electronic spin states [1]. However, in addition to sensitivity to magnetic field, the resonances are also perturbed by inhomogeneities in electric field  $E$ , temperature  $T$ , and crystal strain [20–23]. Due to the symmetry of the NV center, these unwanted perturbations affect the two NV electron spin resonances in the same way and can be eliminated by characterizing both resonances [18, 24].

For wide-field magnetic imaging of time-varying fields, full characterization of the resonance curves at a frame-rate sufficient to capture the magnetic field dynamics may not be possible. In this regime, shifts of one resonance curve can instead be mapped to changes in emitted NV photoluminescence (PL) intensity by applying single-frequency RF excitation [25–27]. This imaging modality enables partial reconstruction of the local magnetic field with a higher frame-rate. The double-quantum (DQ) technique, which drives both spin transitions simultaneously by applying a two-tone RF pulse, eliminates pixel-to-pixel fluctuations of the transition resonant frequencies [18, 24]. However, variations of the shape of the resonance curve also cause changes in the emitted PL intensity, limiting magnetic sensitivity. These variations arise from inhomogeneities in NV and other paramagnetic spin densities as well as external fields [16]. By expanding to a four-tone double-double quantum (DDQ) driving scheme, we suppress curve-shape variations across an imaging field of view. We show both theoretically and experimentally that the DDQ signal is linearly proportional to the magnetic field projection along the NV symmetry axis.

\* zeeshawn@uw.edu

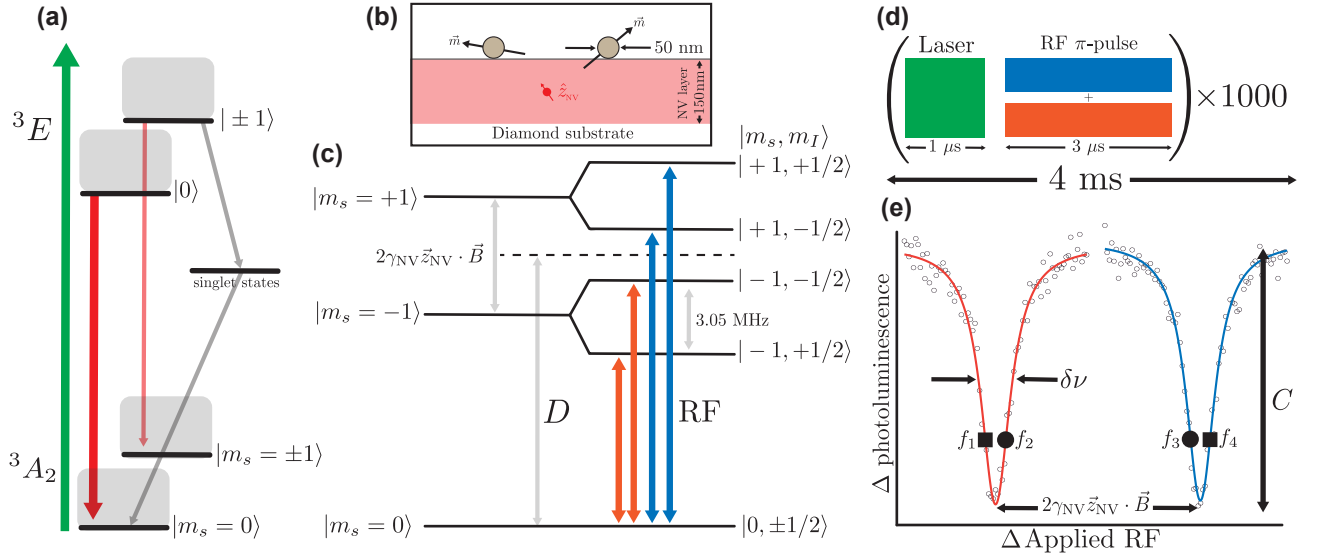


FIG. 1: Wide-field pulsed magnetic imaging using an NV ensemble. (a) NV electronic energy level diagram showing the ground, excited spin states ( $|m_s = 0\rangle, |m_s = \pm 1\rangle$ ), singlet states, optical excitation (green arrow), emitted photoluminescence (red arrow), and spin-selective, non-radiative inter-system-crossing (gray arrows). (b) Schematic showing 50 nm ferromagnetic nanoparticles adhered to the diamond surface. The magnetic moments of the particles are oriented randomly. The 150 nm NV layer (pink) is fabricated on top of the diamond substrate (white), and a single NV pointed along the (111) orientation is shown (red). (c) NV ground state energy level diagram showing the zero-field splitting ( $D$ ), Zeeman splitting of the  $|m_s = \pm 1\rangle$  states ( $2\gamma_{\text{NV}}z_{\text{NV}} \cdot \vec{B}$ ), and  $^{15}\text{N}$ -NV hyperfine splitting (3.05 MHz). RF excitation (orange and blue arrows) rotates the NV spin between the  $|m_s = 0\rangle$  and  $|m_s = \pm 1\rangle$  states. Two-tone RF excitation is simultaneous driven over the two  $^{15}\text{N}$ -NV hyperfine transitions for each NV electron spin state. (d) Laser pulses and multi-tone RF  $\pi$ -pulses are applied repeatedly during a single sCMOS camera exposure. This enables pulsed NV ensemble control in wide-field imaging. (e) By scanning radio-frequency over a spin-transition, a Lorentzian-shaped reduction in NV photoluminescence is observed. Simultaneous driving of the two hyperfine transitions results in a single combined resonance for each  $|m_s = 0\rangle \leftrightarrow |m_s = \pm 1\rangle$  electron spin transition. The resonances are Zeeman split by the external magnetic field. The outer (inner) inflection points  $f_1, f_4$  ( $f_2, f_3$ ) are denoted by black squares (circles). For the resonance curves shown, the FWHM linewidth  $\delta\nu = 300$  kHz and fractional optical contrast  $C = 0.03$ , with optical pulse = 500 ns, RF pulse = 3500 ns, photon collection rate =  $1.1 \times 10^7$  Hz from a  $1 \mu\text{m}^2$  pixel ( $0.15 \mu\text{m}^3$  voxel), and integration time per data point = 144 ms.

## EXPERIMENTAL METHODS

The wide-field NV magnetic particle imaging (magPI) platform used in this work utilizes a near-surface, high density NV ensemble [Fig. 1(b)]. A 150 nm  $^{15}\text{N}$  doped, isotope-purified (99.999%  $^{12}\text{C}$ ) layer was grown by chemical vapor deposition on an electronic-grade diamond substrate (Element Six). The sample was implanted with 25 keV  $\text{He}^+$  at a dose of  $5 \times 10^{11}$  ions/ $\text{cm}^2$  to form vacancies, followed by a vacuum anneal at 900 °C for 2 hours for NV formation and an anneal in  $\text{O}_2$  at 425 °C for 2 hours for charge state stabilization [15]. The resulting ensemble has NV density of  $1.7 \times 10^{16} \text{ cm}^{-3}$  and ensemble spin coherence time  $T_2^* = 2.5 \mu\text{s}$  (Appendix A).

The NV electronic structure and optical and RF control are summarized in Fig. 1. A 532 nm laser pulse (excitation area  $(40 \mu\text{m})^2$ ) is used to optically pump the NV ensemble into the  $|m_s = 0\rangle$  triplet ground state. RF excitation drives transitions from this ground state into the  $|m_s = \pm 1\rangle$  spin states. Optical excitation from the  $|m_s =$

$\pm 1\rangle$  states results in a reduction of PL intensity due to a spin selective, nonradiative inter-system-crossing [28]. This relaxation provides the spin-dependent PL contrast and initialization into the  $|m_s = 0\rangle$  state. Monitoring the emitted PL as a function of radio frequency enables measurement of ODMR for each spin transition [Fig. 1(e)].

From a Lorentzian-shaped resonance curve [see Fig. 1(e)], the shot-noise-limited dc magnetic sensitivity is given by

$$\eta \approx \frac{1}{\gamma_{\text{NV}}} \frac{\delta\nu}{C\sqrt{N}}, \quad (1)$$

where  $C$  is the optical contrast (fractional depth of the resonance curve),  $\delta\nu$  is the full width at half maximum (FWHM) linewidth,  $\gamma_{\text{NV}}$  is the NV gyromagnetic ratio (28 MHz/mT) and  $N$  is the photon detection rate [1]. In the magPI platform, the sensitivity  $\eta \approx 80 \text{ nT}/\sqrt{\text{Hz}}$  from a  $1 \mu\text{m}^2$  pixel ( $0.15 \mu\text{m}^3$  voxel). All three sensor parameters  $C$ ,  $\delta\nu$ , and  $N$  vary across the imaging field of view.

Optical power broadening of the resonance curve is eliminated by using pulsed excitation in which optical and RF fields are applied separately [29]. Optical pulses and RF  $\pi$ -pulses (both  $\mu$ s-scale) are applied to the ensemble repeatedly to fill a sCMOS camera exposure (ms-scale). Each camera exposure is taken with a single set of radio frequencies with a fixed pulse duration [Fig. 1(d)], enabling pulsed NV ensemble control and readout with wide-field camera exposure times [30].

RF excitation is delivered via a broadband microwave antenna with transmission resonance at the NV zero-field-splitting  $D$  [31]. Each radio frequency applied is mixed to create two equal tones separated by 3.05 MHz, which enables simultaneous driving of the two  $^{15}\text{N}$ -NV hyperfine transitions [32] [Fig. 1(c)] and produces one combined resonance for each  $|m_s = 0\rangle \leftrightarrow |m_s = \pm 1\rangle$  transition [Fig. 1(e)]. Samarium cobalt ring magnets (SuperMagnetMan) are used to apply a 1 mT static external magnetic field along the (111) NV orientation. More details about the experimental set up can be found in Appendix B.

To demonstrate the DDQ technique, we use the magPI platform to image the dipolar magnetic field produced by 50 nm dextran coated  $\text{CoFe}_2\text{O}_4$  ferromagnetic nanoparticles (micromod Partikeltechnologie) deposited onto the diamond sensor surface [Fig. 1(b)]. These bio-compatible particles produce nano-scale magnetic fields which lie in the dynamic range of the NV sensing ensemble defined by  $\delta\nu$  of the resonance curves. For other imaging applications, the sensor dynamic range can be increased at the expense of magnetic sensitivity by RF broadening the resonance curve.

## STATIC MAGNETIC IMAGING MODALITY

For static fields, the full NV resonance curve can be measured in wide-field with arbitrarily long acquisition times. Taking a series of PL images over a range of radio-frequencies allows fitting of the entire resonant response in the measured range. Mapping the fitted resonant frequency at each pixel results in a partial reconstruction of the magnetic field as seen in Fig. 2(a). Subtraction of both  $|m_s = 0\rangle \leftrightarrow |m_s = \pm 1\rangle$  resonant frequency maps eliminates shifts of the resonance due to fields other than the magnetic field, and enables imaging of the absolute magnetic field projection along the NV symmetry axis [33], as seen in Fig. 3(a).

For quickly-varying magnetic fields, measurement of the full resonance curve may not be possible. We thus require a dynamic imaging modality that reproduces the absolute magnetic field across the imaging field of view and is compatible with high frame-rate imaging.

## DYNAMIC MAGNETIC IMAGING MODALITIES

### Single Quantum Difference Imaging

The simplest dynamic imaging modality uses RF excitation applied at one inflection point of the resonance curve [Fig. 1(d)]. PL images taken with RF  $\pi$ -pulse applied are subtracted from PL images taken without RF to detect changes in emitted NV PL [27]. We define a single quantum (SQ) difference image (DI) as

$$\text{SQ}(f_1) = \frac{I_{\text{off}} - I_{\text{on}}(f_1)}{I_{\text{off}}}, \quad (2)$$

in which  $I_{\text{on}}(f_1)$  is the intensity image taken with applied RF  $\pi$ -pulses and  $I_{\text{off}}$  is the image taken with no applied RF. In the linear regime of the resonance curve (Appendix D), the per-pixel signal is given by

$$\text{SQ}^{\text{PP}}(f_1) = \frac{9}{8}C - \frac{3\sqrt{3}}{4} \frac{C}{\delta\nu} (\nu(\vec{E}, \vec{B}, \dots) - f_1). \quad (3)$$

As discussed above, the resonant frequency  $\nu$  depends on the magnetic field  $\vec{B}$  and also varies with local electric field  $\vec{E}$ , temperature  $T$ , and crystal strain.

Additionally, variations in curve-shape, and thus  $C$  [Fig. 2(b)] and  $\delta\nu$  [Fig. 2(c)], cause fluctuations of the resonance curve inflection point, contributing to the SQ signal. Microscopic and mesoscopic strain inhomogeneities result in inhomogeneous broadening of the resonance curve [8]. Additionally, dephasing due to dipolar interactions between sensor NV centers and other paramagnetic impurities (e.g. P1 and NV) fundamentally limit the NV ensemble coherence, and thus, ODMR linewidth [15, 16]. Further fluctuations of effective NV density in the magPI platform arise from interrogating one of four randomly distributed NV crystallographic orientations [1].

The SQ DI enables imaging of some nano-scale magnetic structure, but the sensitivity of this technique is limited. In Fig. 3(b) we show a SQ DI image with its corresponding static magnetic field map in 3(a). The SQ DI enables partial mapping of the magnetic field projection, but because the SQ modality is sensitive to external fields, not all structures in the SQ DI correspond to magnetic field projection signal.

### Double Quantum Difference Imaging

Temperature  $T$ , electric field  $\vec{E}$ , and strain shift the zero-field-splitting of the NV ground state, causing common-mode shifts of the  $|m_s = 0\rangle \leftrightarrow |m_s = \pm 1\rangle$  resonant frequencies [5]. Conversely, the magnetic-field-induced Zeeman effect splits the two resonant frequencies. Thus, by probing the difference of the resonant frequencies, the common-mode shifts can be subtracted out and the magnetic field projection can be measured directly. We use a double-quantum (DQ) driving

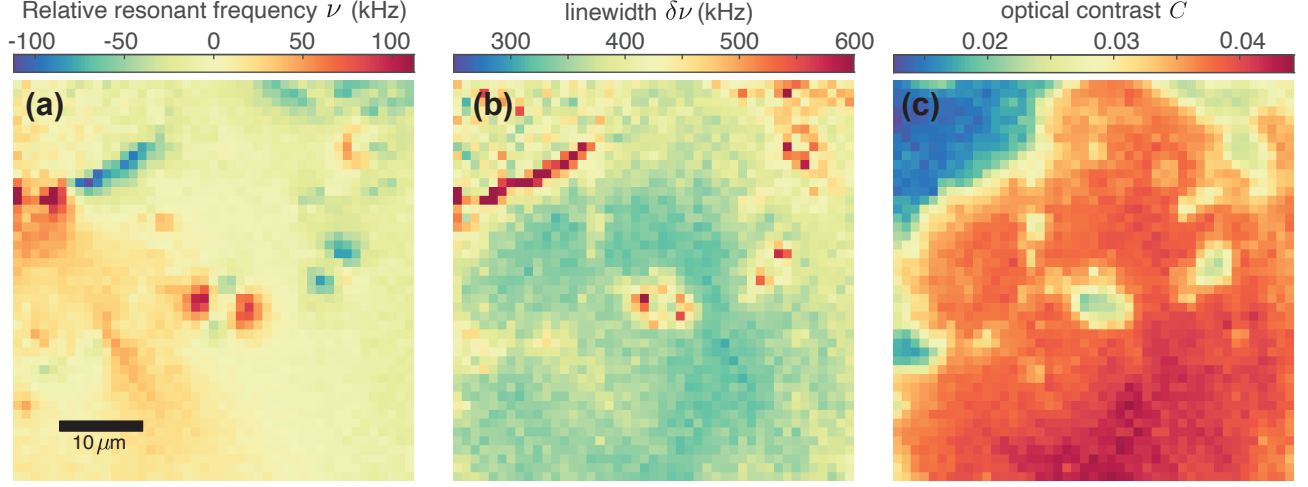


FIG. 2: Resonance curve variation. The  $|m_s = 0\rangle \leftrightarrow |m_s = -1\rangle$  NV ODMR is measured in wide-field and each pixel's resonance curve is fit to a Lorentzian. (a) Variation in fitted resonant frequency. Shifts associated with magnetic dipoles as well as strain features are visible. (b) Variation of fitted FWHM linewidth  $\delta\nu$ . Inhomogenous broadening due to the gradient of magnetic dipole and strain fields results in an increase of  $\delta\nu$  and decrease of  $C$ . (c) Variation of fitted fractional optical contrast  $C$ .

scheme [17, 24], applying two-tone RF  $\pi$ -pulses at the opposite inflection points of the two resonance curves [Fig. 1(e)]. We construct a DQ DI by subtracting the PL image taken with double-quantum RF driving from an image taken with no RF applied, giving a signal of

$$\text{DQ}(f_1, f_4) = \frac{I_{\text{off}} - I_{\text{on}}(f_1, f_4)}{I_{\text{off}}}, \quad (4)$$

in which  $I_{\text{on}}(f_1, f_4)$  is the image taken with applied RF  $\pi$ -pulses, and  $I_{\text{off}}$  is the image taken with no applied RF. Working in the linear regime of each resonance curve (Appendix D) and assuming that the two resonance curves are the same shape, the per-pixel signal is

$$\begin{aligned} \text{DQ}^{\text{PP}}(f_1, f_4) \approx & \frac{9}{4}C - \frac{3\sqrt{3}}{4} \frac{C}{\delta\nu} (f_1 - f_4) \\ & - \frac{3\sqrt{3}}{4} \frac{C}{\delta\nu} (2\gamma_{\text{NV}} \hat{z}_{\text{NV}} \cdot \vec{B}), \end{aligned} \quad (5)$$

where  $\vec{B}$  is the local magnetic field and  $\hat{z}_{\text{NV}}$  is the NV ensemble symmetry axis. By defining  $\langle \vec{B} \rangle$  as the average magnetic field over the imaging field of view, Eq. 5 simplifies to

$$\begin{aligned} \text{DQ}^{\text{PP}}(f_1, f_4) = & \frac{9}{4}C + \frac{3\sqrt{3}}{4} \frac{C}{\delta\nu} 2\delta_0 \\ & - \frac{3\sqrt{3}}{4} \frac{C}{\delta\nu} \left( 2\gamma_{\text{NV}} \hat{z}_{\text{NV}} \cdot (\vec{B} - \langle \vec{B} \rangle) \right), \end{aligned} \quad (6)$$

where  $2\delta_0 = (f_4 - f_1) - 2\gamma_{\text{NV}} \hat{z}_{\text{NV}} \cdot \langle \vec{B} \rangle$ . By applying  $f_1$  and  $f_4$  at the outer inflection points of the NV resonance curves [Fig. 1(e)], intensity changes induced by non-magnetic, common-mode shifts are cancelled out,

while splittings caused by magnetic signal result in a sum of changes in PL intensity. Hence, for constant  $C$  and  $\delta\nu$ , the DQ DI technique enables absolute magnetic imaging. [24]

While the dependence of the resonant frequency on external fields has been suppressed, the limitations imposed by curve-shape persist for DQ imaging. The variations of  $C$  and  $\delta\nu$  still cause fluctuations in the first two terms in Eq. 6. Comparison of the DQ DI in Fig. 3(c) to the magnetic field projection map in Fig. 3(a) highlights this limited correlation. While eliminating the limiting factor of the SQ modality, DQ DI has *increased* the effect of variations in curve-shape on the magnetic imaging, which can be seen by comparing the map of  $C$  in Fig. 2(c) with the DQ DI in Fig. 3(c).

### Double-Double Quantum Difference Imaging

To suppress the imaging dependence on the shape of the resonance curve, we construct a double-double quantum (DDQ) DI

$$\text{DDQ} = 2 \frac{I_{\text{on}}(f_1, f_4) - I_{\text{on}}(f_2, f_3)}{I_{\text{on}}(f_1, f_4) + I_{\text{on}}(f_2, f_3)}, \quad (7)$$

where  $I_{\text{on}}(f_1, f_4)$  ( $I_{\text{on}}(f_2, f_3)$ ) is the image taken with RF applied at the outer (inner) inflection points of the two resonance curves as denoted in Fig. 1(e).

Because of the choice of RF, the per-pixel DDQ signal simplifies in a similar manner as the DQ signal in Eq. 6

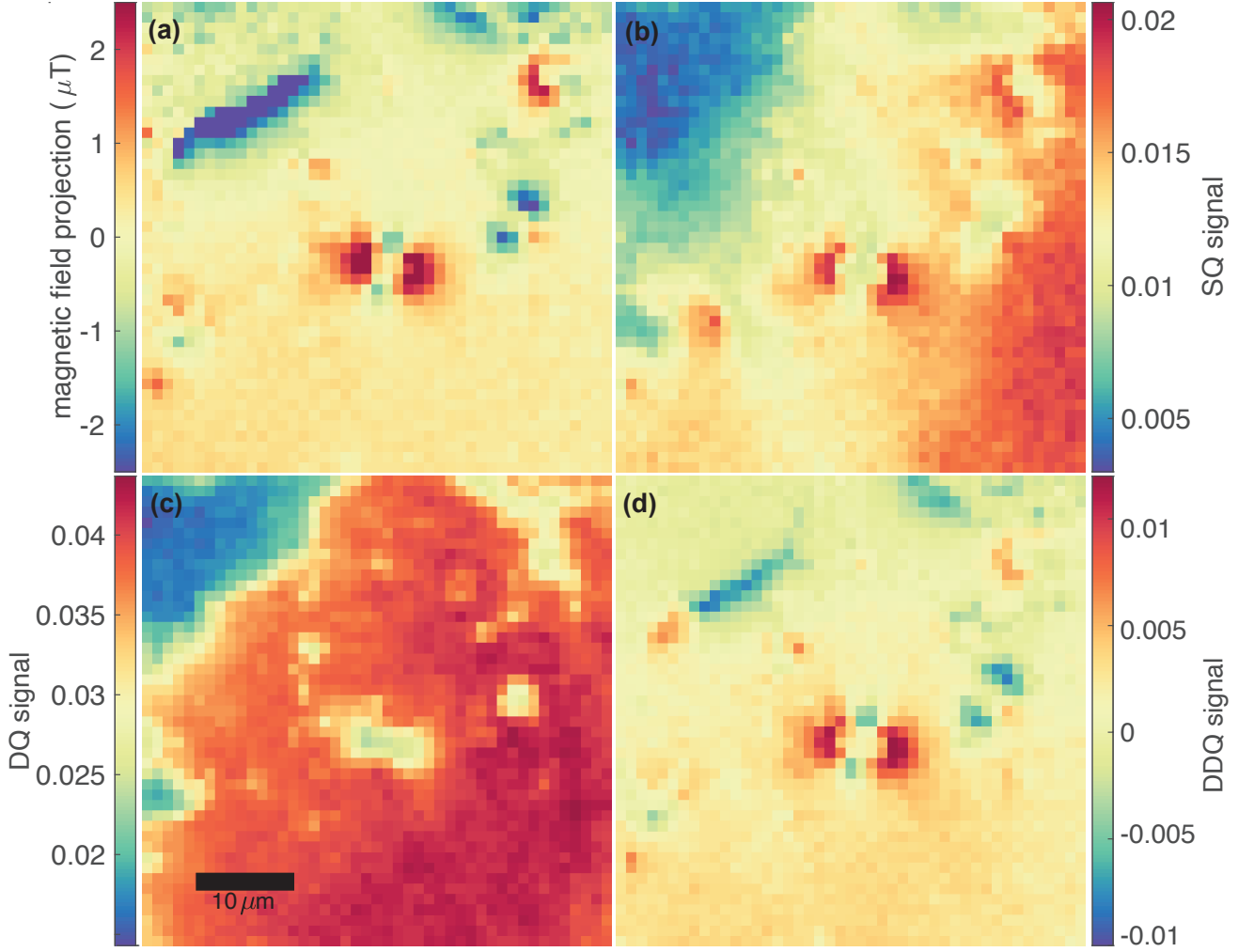


FIG. 3: Magnetic imaging modality comparison. (a) Static magnetic field projection map. NV ODMR is measured for each  $|m_s = 0\rangle \leftrightarrow |m_s = \pm 1\rangle$  electronic spin transition. The two resonant frequencies are subtracted and divided by the NV gyromagnetic ratio  $\gamma_{\text{NV}}$ , reconstructing a map of the magnetic field projection. (acquisition time 12 seconds) (b) Single quantum (SQ) difference image (DI) with RF  $\pi$ -pulses applied at the inflection point  $f_1$  of the  $|m_s = 0\rangle \leftrightarrow |m_s = -1\rangle$  resonance. Inhomogeneities in the SQ magnetic signal are greater than the dipolar magnetic field signal. (acquisition time 2.4 seconds) (c) Double quantum difference image with RF  $\pi$ -pulses applied at outer inflection points  $f_1$  and  $f_4$ . (acquisition time 2.4 seconds) (d) Double-double quantum difference image with RF  $\pi$ -pulses applied at outer inflection points  $f_1$  and  $f_4$ , subtracted from an image with RF  $\pi$ -pulses applied at inner inflection points  $f_2$  and  $f_3$ . Inhomogeneities in external magnetic, electric and strain fields are suppressed, and the DDQ signal is proportional to magnetic field projection (a). (acquisition time 2.4 seconds)

giving the per-pixel signal of

$$\text{DDQ}^{\text{PP}} \approx \frac{\frac{3\sqrt{3}}{2} \frac{C}{\delta\nu}}{1 - \left(\frac{9}{4} - \frac{3\sqrt{3}}{2} \frac{\delta\omega}{\delta\nu}\right)C} \left(2\gamma_{\text{NV}} \hat{z}_{\text{NV}} \cdot (\vec{B} - \langle \vec{B} \rangle)\right). \quad (8)$$

Uncertainty on the per-pixel DDQ signal in Eq. 8 due to shot noise and the simplifying assumptions listed before Eq. 5 is discussed in Appendix E. DDQ eliminates the first two terms of the DQ DI signal Eq. 6 to obtain a single term which is linearly proportional to  $(\vec{B} - \langle \vec{B} \rangle)$ . There is still multiplicative dependence on  $C$  and  $\delta\nu$ ,

but because the shift of the resonant frequency far from magnetic field sources falls off faster than the impact of spatial variations of curve-shape, there is no longer false signal generated in regions with no magnetic field. The DDQ image completely eliminates the large-scale, non-magnetic-field-generated gradients in the SQ difference image [Fig. 3(b)] and suppresses the  $C$  and  $\delta\nu$  dependence [Fig. 2(b-c)] of the DQ DI [Fig. 3(c)]. As shown in Fig. 3(d), DDQ DI provides similar magnetic sensitivity as the full magnetic projection map in Fig. 3(a), with a  $>4$ -fold acquisition time reduction. The static

imaging modality requires enough images to fit both resonance curves; the DDQ modality instead extracts the magnetic field dependence of the resonances with only two images:  $I_{\text{on}}(f_1, f_4)$  and  $I_{\text{on}}(f_2, f_3)$ . While the integration time of the DDQ image shown in Fig. 3(d) was chosen to match the signal to noise ratio of the magnetic field map in Fig. 3(a), DDQ enables even faster magnetic imaging (Appendix C).

## CONCLUSION AND OUTLOOK

The NV community has made significant progress toward eliminating inhomogeneities in NV sensor ensembles, both through advanced sensor fabrication [10] and quantum control methods [16]. Here, we introduce a new quantum control technique, double-double quantum difference imaging, that is suitable for wide-field dc magnetic imaging of time-varying fields. Using four-tone RF pulses and only a two-image sequence, we show both theoretically and experimentally that DDQ difference imaging not only mitigates perturbations of the sensor resonant frequency but also variations of resonance curve-shape. We illustrate that these resonance shape variations can be the dominant source of imaging noise in a state-of-the-art NV magnetic imaging surface. For ease of adoption, we further emphasize that DDQ eliminates the need for per-pixel calibration and enables absolute magnetic imaging via NV photoluminescence intensity imaging. Due to the combined performance enhancement and ease of use, we expect the DDQ DI technique to advance real-time, video-rate magnetic imaging applications, such as magnetic moment orientation tracking of magnetic nanoparticles.

## ACKNOWLEDGEMENTS

This material is based on work supported by the National Science Foundation under Grant No. 1607869. Helium ion implantation measurements were carried out at the Environmental and Molecular Sciences Laboratory, a national scientific user facility sponsored by DOE's Office of Biological and Environmental Research and located at Pacific Northwest National Laboratory (PNNL). PNNL is a multiprogram laboratory operated for DOE by Battelle under Contract DE-AC05-76RL01830. K.M.I. acknowledges support from the Spintronics Research Network of Japan. I. M. S. conceptualized the work; Z.K. conducted the experiments.

### Appendix A: NV ensemble properties

The near-surface NV ensemble used in this work was fabricated using the protocol detailed in the main text as well as Ref. [15]. After fabrication, confocal images of the sensor were compared to single NV confocal images

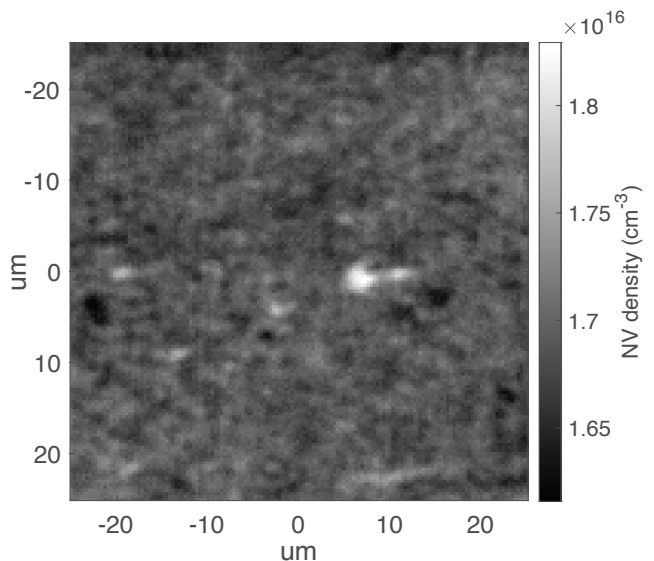


FIG. A1: Confocal image showing varying NV density across the sensor surface. NV density was calibrated by measuring the single NV photoluminescence signal using the same optical settings. Optical power = 2.4 mW, spot size 1.185  $\mu\text{m}$ .

to determine the average NV density of  $1.7 \times 10^{16} \text{ cm}^{-3}$  [Fig. A1]. To estimate the coherence time of the NV ensemble, we perform a Ramsey interferometry measurement [Fig. A2]. We measure  $T_2^* = 2.5 \mu\text{s}$  from a collection volume  $2700 \mu\text{m}^3$ . We note that the  $T_2^*$  does not increase by sampling from a smaller collection volume, indicating low inhomogeneous broadening of the NV resonance across our imaging area.

### Appendix B: Experimental setup

Green light from a laser (Laser Quantum opus532) is intensity modulated by an acousto-optical modulator (AOM) (Gooch & Housego 3080-294), expanded, and focused onto the back focal plane of an objective lens (Nikon LU Plan Fluor 100x NA 0.9). NV photoluminescence is collected by the objective, filtered to remove laser reflection (Semrock BLP02-561R-25) and imaged onto a sCMOS camera (Hamamatsu OrcaFlash C13440-20CU).

RF excitation is generated by two two-channel RF generators (WindFreak SynthNV and SynthHDPPro). The two-channels are combined (MiniCircuits ZX10-2-42-S+) and modulated by an RF switch (MiniCircuits ZFSWA2-63DR+). The signals are mixed (Pasternack PE8650) to generate a two-tone RF signal that can simultaneously drive the two  $^{15}\text{N}$ -NV hyperfine transitions. The signal is amplified (MiniCircuits ZHL-4240W+) and delivered to the NV ensemble via a broadband microwave antenna. A pulse generator (PulseBlaster ESR Pro 500 MHz) triggers the RF switch, AOM, and camera exposures.

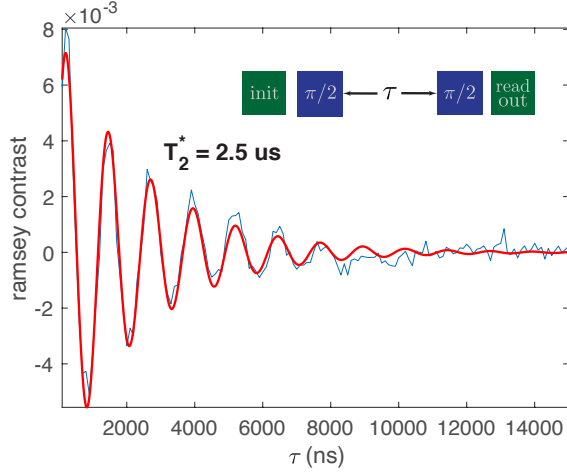


FIG. A2: Ramsey fringes of the NV ensemble (collection volume  $2700 \mu\text{m}^3$ ). Here, the free evolution time  $\tau$  is the time between the end of the first RF pulse and the beginning of the second RF pulse. The fringes are fit to an exponentially damped sinusoid to determine the ensemble coherence time  $T_2^* = 2.5 \mu\text{s}$ . The inset shows the pulse sequence used, where green denotes optical pulse (500 ns) and blue RF pulse (500 ns). The RF excitation is detuned by 600 kHz.

### Appendix C: Acquisition time comparison

While the DDQ integration time in the main text data was chosen to match the signal-to-noise ratio of the full magnetic field map, we note that magnetic field detection can occur at much shorter timescales. In Fig. A3 we demonstrate the DDQ technique enabling imaging of nano-scale magnetic signals with substantially smaller integration times than the static frequency scan imaging modality. Due to the suppression of external field and curve shape dependence, we anticipate that DDQ imaging will eventually enable video-rate imaging of time-varying nano-scale magnetic fields.

### Appendix D: Derivation of SQ, DQ, and DDQ Difference Image Signals

The Lorentzian-shaped NV resonance curves [see Fig. 1(d)] can be described by

$$I(f) = 1 - \frac{C}{\left(\frac{\nu-f}{\delta\nu/2}\right)^2 + 1}, \quad (\text{D1})$$

where  $C$  is the optical contrast,  $\nu$  is the resonant frequency,  $\delta\nu$  is the FWHM linewidth of the curve and  $f$  is the applied radio frequency. We approximate the resonance curve by Taylor expanding to first order around the inflection point on either side of the curve. In this

linear regime, the NV resonance is given by

$$I(f) \approx 1 - \frac{9}{8}C + \frac{3\sqrt{3}}{4} \frac{C}{\delta\nu} |\nu - f|. \quad (\text{D2})$$

#### 1. Single Quantum Difference Imaging (SQ DI)

The SQ signal in Eq. 3 directly follows from the linear approximation in Eq. D2.

#### 2. Double Quantum Difference Imaging (DQ DI)

For DQ DI, due to simultaneously interrogating both the  $|m_s = 0\rangle \leftrightarrow |m_s = \pm 1\rangle$  transitions, the linear approximation to the response is given by

$$I(f_1, f_4) \approx 1 - \frac{9}{8}C_- + \frac{3\sqrt{3}}{4} \frac{C_-}{\delta\nu_-} (\nu_- - f_1) \dots - \frac{9}{8}C_+ + \frac{3\sqrt{3}}{4} \frac{C_+}{\delta\nu_+} (-\nu_+ + f_4), \quad (\text{D3})$$

in which the  $\pm$  subscripts refer to the  $|m_s = 0\rangle \leftrightarrow |m_s = \pm 1\rangle$  resonance curves. By applying the RF of the same Rabi frequency to both resonances, we simplify the signal to

$$I(f_1, f_4) \approx 1 - \frac{9}{4}C + \frac{3\sqrt{3}}{4} \frac{C}{\delta\nu} (-\nu_+ + \nu_- + (f_4 - f_1)), \quad (\text{D4})$$

where  $C$  and  $\delta\nu$  refer to the contrast and linewidth of both resonance curves needed for the measurement. The effect of mismatched contrasts and linewidths of the two resonance curves is addressed in Appendix E. The applied frequencies  $f_1$  and  $f_4$  are chosen to be at the outer inflection points of the average pixel in an empty field of view. The difference in resonant frequencies is proportional to the local magnetic field, giving the form found in Eq. 6.

If the inner inflection points are chosen, the DQ DI signal is given by:

$$I(f_2, f_3) \approx 1 - \frac{9}{4}C + \frac{3\sqrt{3}}{4} \frac{C}{\delta\nu} (\nu_+ - \nu_- + (f_2 - f_3)). \quad (\text{D5})$$

#### 3. Double-Double Quantum Difference Imaging (DDQ DI)

Taking the difference between Eq. D4 and the Eq. D5, we see the constant term and term that only depends on  $C$  vanish. The resulting DDQ DI signal is

$$I \approx \frac{3\sqrt{3}}{4} \frac{C}{\delta\nu} (2(\nu_+ - \nu_-) - (f_4 + f_3 - f_2 - f_1)). \quad (\text{D6})$$

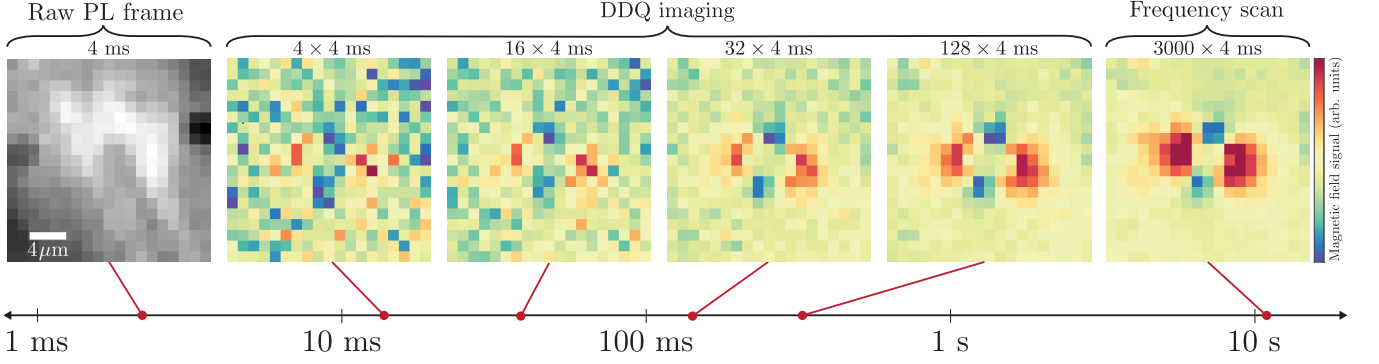


FIG. A3: Magnetic imaging frame rate comparison. A minimum-exposure raw photoluminescence (PL) frame is shown on the left. DDQ images with increasing integration time are compared to a static magnetic field map. DDQ imaging enables a comparable signal to noise as the static frequency scan imaging modality with substantially smaller integration times.

By choosing applied frequencies such that  $f_4 + f_3 - f_2 - f_1 = \Delta f = 2\gamma_{\text{NV}}\hat{z}_{\text{NV}} \cdot \langle \vec{B} \rangle$ , and dividing by the average of Eq. D4 and the Eq. D5, we reproduce Eq. 8. The division controls for temporal fluctuations of laser power reaching the diamond as well as spatial differences in collected photon rate.

To simplify the DDQ signal slightly, we can instead normalize the DDQ image by an RF-off photoluminescence image

$$\text{DDQ} = \frac{I(f_1, f_4) - I(f_2, f_3)}{I_{\text{off}}}, \quad (\text{D7})$$

which simplifies to

$$\text{DDQ}^{\text{pp}} \approx \frac{3\sqrt{3}}{2} \frac{C}{\delta\nu} \left( 2\gamma_{\text{NV}}\hat{z}_{\text{NV}} \cdot (\vec{B} - \langle \vec{B} \rangle) \right). \quad (\text{D8})$$

Equations D7 and D8 provide a simpler mathematical form of the DDQ signal with a three-image instead of a two-image sequence.

### Appendix E: Estimation of Signal and Error Analysis

Errors in all difference imaging signals arise from a variety of sources. For the photon collection rates of interest, difference imaging will be fundamentally limited by photon shot noise. For the images shown in the main text, we measure on average  $4.4 \times 10^4$  counts per 4 ms frame ( $11 \times 10^6$  counts per second) from a  $1 \mu\text{m}^2$  pixel ( $0.15 \mu\text{m}^3$  voxel). Here, we examine and quantify other sources of error in the DDQ signal and relate them to the shot noise floor.

#### 1. Shot noise

Shot noise impacts all PL images necessary for DDQ imaging. Recall the equation for the simplified DDQ DI,

$$\text{DDQ}(x, y) = \frac{I_{\text{on}}(f_2, f_3, x, y) - I_{\text{on}}(f_1, f_4, x, y)}{I_{\text{off}}(x, y)}, \quad (\text{E1})$$

where we now insert explicit  $xy$ -dependence to specify the counts for an individual pixel. We treat the distribution of photon counts as a normal distribution with mean and variance equal to expected number of photons counted from that pixel. Combining normal distributions gives us a predicted variance on the per-pixel DDQ signal of

$$\sigma_{\text{DDQ}}^2 = \left( \frac{\bar{I}_{\text{on}}(f_2, f_3, x, y) - \bar{I}_{\text{on}}(f_1, f_4, x, y)}{\bar{I}_{\text{off}}(x, y)} \right)^2 \times \left[ \frac{\bar{I}_{\text{on}}(f_2, f_3, x, y) + \bar{I}_{\text{on}}(f_1, f_4, x, y)}{(\bar{I}_{\text{on}}(f_2, f_3, x, y) - \bar{I}_{\text{on}}(f_1, f_4, x, y))^2} + \frac{\bar{I}_{\text{off}}(x, y)}{(\bar{I}_{\text{off}}(x, y))^2} \right], \quad (\text{E2})$$

where all  $\bar{I}$ 's refer to the mean number of photons detected for the pixel located at  $(x, y)$  for an image. Equation E2 can be rearranged to

$$\sigma_{\text{DDQ}}^2 = \frac{\bar{I}_{\text{on}}(f_2, f_3, x, y) + \bar{I}_{\text{on}}(f_1, f_4, x, y)}{(\bar{I}_{\text{off}}(x, y))^2} \times \left[ 1 + \frac{(\bar{I}_{\text{on}}(f_2, f_3, x, y) - \bar{I}_{\text{on}}(f_1, f_4, x, y))^2}{\bar{I}_{\text{off}}(x, y) \times (\bar{I}_{\text{on}}(f_2, f_3, x, y) + \bar{I}_{\text{on}}(f_1, f_4, x, y))} \right]. \quad (\text{E3})$$

In ensemble NV sensing in which all 4 NV orientations are present, the optical contrast of the a resonance curve corresponding to a single NV orientation is always less than 0.08. Thus, the second term in the brackets of Eq. E3 is on the order of  $10^{-4}$ . Neglecting the second term and

approximating  $\bar{I}_{\text{on}}$  as  $\bar{I}_{\text{off}}$  due to small  $C$ , a lower bound on the variance of the DDQ signal due to the shot noise is given by

$$\sigma_{\text{DDQ}}^2 \approx \frac{2}{\bar{I}_{\text{off}}(x, y)}. \quad (\text{E4})$$

For a signal to noise ratio (SNR) of 1, this requires around  $2 \times 10^4$  counts per pixel, or an integration time of 1.8 ms for a  $1 \mu\text{m}^2$  pixel ( $0.15 \mu\text{m}^3$  voxel). In the magPI platform, the minimum camera exposure time is 4 ms, giving us a SNR of  $>1$  per PL frame. In the remainder of this appendix, we will examine what integration times are required for the shot noise SNR to fall below other sources of noise.

## 2. Linear Approximation Error

Finding absolute magnetic field from the DDQ signal relies on the linear approximation of the Lorentzian resonance curve. Shifts within  $(1/3) \times \delta\nu$  of the inflection points limit the error due to nonlinearity to under 5%. As  $\delta\nu$  is tunable by changing the power of the RF  $\pi$ -pulses, if larger magnetic field variations need to be measured, one can RF-broaden  $\delta\nu$  to reduce this error. In this study, we observe resonant frequency shifts  $<100$  kHz, as seen in Fig. 2(a), with  $\delta\nu$  of 300 kHz, as seen in Fig. 1(e). For outlier values around 100 kHz in Fig. 2(a), we find the error due to non-linearity to be less than 5%. Shot-noise exceeds this contribution for integration times of at least 720 ms ( $8 \times 10^6$  counts per pixel).

## 3. In-Pixel Curve Shape Matching Error

Both DQ DI and DDQ DI assume that equal shifts of the two resonance curves lead to shifts of equal magni-

tude in relative intensity. For this to hold, the curve-shape of each resonance curve used must be the same. From Eq. D3 to Eq. D4, the contrasts  $C_{\pm}$  and linewidths  $\delta\nu_{\pm}$  are assumed identical. By not having perfectly identical RF  $\pi$ -pulses for the two transitions, we observe a difference in  $C_{\pm}$  and  $\delta\nu_{\pm}$  of the resonance curves. The error introduced by this is given by

$$\begin{aligned} \frac{C_{\pm}}{\delta\nu_{\pm}} &= \frac{\bar{C}(1 \pm r_C)}{\bar{\delta\nu}(1 \pm r_{\delta\nu})} \\ &\approx \frac{\bar{C}}{\bar{\delta\nu}} (1 \pm r_C \mp r_{\delta\nu} - r_C r_{\delta\nu} + r_{\delta\nu}^2 \pm r_{\delta\nu}^2 r_C \dots \\ &\quad \mp r_{\delta\nu}^3 + r_{\delta\nu}^4 - r_C r_{\delta\nu}^3 + \mathcal{O}(r^5)), \quad (\text{E5}) \end{aligned}$$

in which  $r_C = (C_+ - C_-)/(C_+ + C_-)$ ,  $r_{\delta\nu} = (\delta\nu_+ - \delta\nu_-)/(\delta\nu_+ + \delta\nu_-)$ ,  $\bar{C} = (1/2)(C_+ + C_-)$ , and  $\bar{\delta\nu} = (1/2)(\delta\nu_+ + \delta\nu_-)$ .  $C_{\pm}$  and  $\delta\nu_{\pm}$  are the contrast and linewidth for the resonance curve for each  $|m_s = 0\rangle \leftrightarrow |m_s = \pm 1\rangle$  transition. Because these errors enter additively, only the even order terms survive, giving us the contribution to the error on a DDQ DI:

$$DDQ(f_1, f_2, f_3, f_4) \times 2 [r_{\delta\nu}^2 - r_C r_{\delta\nu} + \mathcal{O}(r^4)] \quad (\text{E6})$$

As this error is proportional to the DDQ signal, its SNR is independent of counts. For a typical field of view,  $|r_C| < 0.1$  and  $|r_{\delta\nu}| < 0.1$ , thus the term  $r_{\delta\nu}^2 - r_C r_{\delta\nu}$  is bounded by 0.04. This corresponds to a conservative estimate of the SNR for mismatched curve shape of 25. For the contribution due to shot noise to be of the same order, we require  $5 \times 10^7$  counts per pixel. In this experiment, that corresponds an integration time of 4.5 s.

- 
- [1] E. Abe and K. Sasaki, Tutorial: Magnetic resonance with nitrogen-vacancy centers in diamond - Microwave engineering, materials science, and magnetometry, *Journal of Applied Physics* **123**, 10.1063/1.5011231 (2018).
  - [2] S. Hong, M. S. Grinolds, L. M. Pham, D. Le Sage, L. Luan, R. L. Walsworth, and A. Yacoby, Nanoscale magnetometry with NV centers in diamond, *MRS Bulletin* **38**, 155 (2013).
  - [3] R. Schirhagl, K. Chang, M. Loretz, and C. L. Degen, Nitrogen-Vacancy Centers in Diamond: Nanoscale Sensors for Physics and Biology, *Annual Review of Physical Chemistry* **65**, 83 (2014).
  - [4] G. Balasubramanian, P. Neumann, D. Twitchen, M. Markham, R. Kolesov, N. Mizuochi, J. Isoya, J. Achard, J. Beck, J. Tissler, V. Jacques, P. R. Hemmer, F. Jelezko, and J. Wrachtrup, Ultralong spin coherence time in isotopically engineered diamond, *Nature Materials* **8**, 383 (2009).
  - [5] E. V. Levine, M. J. Turner, P. Kehayias, C. A. Hart, N. Langellier, R. Trubko, D. R. Glenn, R. R. Fu, and R. L. Walsworth, Principles and techniques of the quantum diamond microscope, *Nanophotonics* 10.1515/nanoph-2019-0209 (2019).
  - [6] J. P. Tettegne, N. Dentschuk, D. A. Broadway, A. Stacey, D. A. Simpson, and L. C. Hollenberg, Quantum imaging of current flow in graphene, *Science Advances* **3**, 10.1126/sciadv.1602429 (2017).
  - [7] J. F. Barry, M. J. Turner, J. M. Schloss, D. R. Glenn, Y. Song, M. D. Lukin, H. Park, and R. L. Walsworth, Optical magnetic detection of single-neuron action potentials using quantum defects in diamond, *PNAS* , 1 (2016).
  - [8] P. Kehayias, M. J. Turner, R. Trubko, J. M. Schloss, C. A. Hart, M. Wesson, D. R. Glenn, and R. L. Walsworth, Imaging crystal stress in diamond using ensembles of nitrogen-vacancy centers, *Physical Review B*

- 100**, 1 (2019).
- [9] Y. Schlussek, T. Lenz, D. Rohner, Y. Bar-Haim, L. Bougas, D. Groswasser, M. Kieschnick, E. Rozenberg, L. Thiel, A. Waxman, J. Meijer, P. Maletinsky, D. Budker, and R. Folman, Wide-Field Imaging of Superconductor Vortices with Electron Spins in Diamond, *Physical Review Applied* **10**, 1 (2018).
- [10] V. M. Acosta, E. Bauch, M. P. Ledbetter, C. Santori, K. M. Fu, P. E. Barclay, R. G. Beausoleil, H. Linget, J. F. Roch, F. Treussart, S. Chemerisov, W. Gawlik, and D. Budker, Diamonds with a high density of nitrogen-vacancy centers for magnetometry applications, *Physical Review B - Condensed Matter and Materials Physics* **80**, 1 (2009).
- [11] K. Ohno, F. Joseph Heremans, C. F. De Las Casas, B. A. Myers, B. J. Alemán, A. C. Bleszynski Jayich, and D. D. Awschalom, Three-dimensional localization of spins in diamond using  $^{12}\text{C}$  implantation, *Applied Physics Letters* **105**, 10.1063/1.4890613 (2014).
- [12] C. Osterkamp, M. Mangold, J. Lang, P. Balasubramanian, T. Teraji, B. Naydenov, and F. Jelezko, Engineering preferentially-aligned nitrogen-vacancy centre ensembles in CVD grown diamond, *Scientific Reports* **9**, 1 (2019).
- [13] T. R. Eichhorn, C. A. McLellan, and A. C. Bleszynski Jayich, Optimizing the formation of depth-confined nitrogen vacancy center spin ensembles in diamond for quantum sensing, *Physical Review Materials* **3**, 1 (2019).
- [14] J. P. Tetienne, R. W. De Gille, D. A. Broadway, T. Teraji, S. E. Lillie, J. M. McCoe, N. Dontschuk, L. T. Hall, A. Stacey, D. A. Simpson, and L. C. Hollenberg, Spin properties of dense near-surface ensembles of nitrogen-vacancy centers in diamond, *Physical Review B* **97**, 1 (2018).
- [15] E. E. Kleinsasser, M. M. Stanfield, J. K. Banks, Z. Zhu, W. D. Li, V. M. Acosta, H. Watanabe, K. M. Itoh, and K. M. C. Fu, High density nitrogen-vacancy sensing surface created via He<sup>+</sup> ion implantation of  $^{12}\text{C}$  diamond, *Applied Physics Letters* **108**, 10.1063/1.4949357 (2016).
- [16] E. Bauch, C. A. Hart, J. M. Schloss, M. J. Turner, J. F. Barry, P. Kehayias, S. Singh, and R. L. Walsworth, Ultralong Dephasing Times in Solid-State Spin Ensembles via Quantum Control, *Physical Review X* **8**, 31025 (2018).
- [17] B. A. Myers, A. Ariyaratne, and A. C. Jayich, Double-Quantum Spin-Relaxation Limits to Coherence of Near-Surface Nitrogen-Vacancy Centers, *Physical Review Letters* **118**, 1 (2017).
- [18] H. J. Mamin, M. H. Sherwood, M. Kim, C. T. Retner, K. Ohno, D. D. Awschalom, and D. Rugar, Multipulse double-quantum magnetometry with near-surface nitrogen-vacancy centers, *Physical Review Letters* **113**, 1 (2014).
- [19] G. De Lange, T. Van Der Sar, M. Blok, Z. H. Wang, V. Dobrovitski, and R. Hanson, Controlling the quantum dynamics of a mesoscopic spin bath in diamond, *Scientific Reports* **2**, 1 (2012).
- [20] F. Dolde, H. Fedder, M. W. Doherty, T. Nöbauer, F. Rempp, G. Balasubramanian, T. Wolf, F. Reinhard, L. C. Hollenberg, F. Jelezko, and J. Wrachtrup, Electric-field sensing using single diamond spins, *Nature Physics* **7**, 459 (2011).
- [21] T. Mittiga, S. Hsieh, C. Zu, B. Kobrin, F. Machado, P. Bhattacharyya, N. Z. Rui, A. Jarmola, S. Choi, D. Budker, and N. Y. Yao, Imaging the Local Charge Environment of Nitrogen-Vacancy Centers in Diamond, *Physical Review Letters* **121**, 1 (2018).
- [22] V. M. Acosta, E. Bauch, M. P. Ledbetter, A. Waxman, L. S. Bouchard, and D. Budker, Temperature dependence of the nitrogen-vacancy magnetic resonance in diamond, *Physical Review Letters* **104**, 1 (2010).
- [23] D. A. Broadway, B. C. Johnson, M. S. Barson, S. E. Lillie, N. Dontschuk, D. J. McCloskey, A. Tsai, T. Teraji, D. A. Simpson, A. Stacey, J. C. McCallum, J. E. Bradby, M. W. Doherty, L. C. Hollenberg, and J. P. Tetienne, Microscopic Imaging of the Stress Tensor in Diamond Using in Situ Quantum Sensors, *Nano Letters* **19**, 4543 (2019).
- [24] K. Fang, V. M. Acosta, C. Santori, Z. Huang, K. M. Itoh, H. Watanabe, S. Shikata, and R. G. Beausoleil, High-Sensitivity Magnetometry Based on Quantum Beats in Diamond Nitrogen-Vacancy Centers, *Physical Review Letters* **130802**, 1 (2013).
- [25] L. M. Pham, D. Le Sage, P. L. Stanwix, T. K. Yeung, D. Glenn, A. Trifonov, P. Cappellaro, P. R. Hemmer, M. D. Lukin, H. Park, A. Yacoby, and R. L. Walsworth, Magnetic field imaging with nitrogen-vacancy ensembles, *New Journal of Physics* **13**, 10.1088/1367-2630/13/4/045021 (2011).
- [26] J. M. McCoe, R. W. de Gille, B. Nasr, J. P. Tetienne, L. T. Hall, D. A. Simpson, and L. C. Hollenberg, Rapid, High-Resolution Magnetic Microscopy of Single Magnetic Microbeads, *Small* **15**, 1 (2019).
- [27] A. M. Wojciechowski, M. Karadas, A. Huck, C. Osterkamp, S. Jankuhn, J. Meijer, F. Jelezko, and U. L. Andersen, Camera-limits for wide-field magnetic resonance imaging with a nitrogen-vacancy spin sensor, *Review of Scientific Instruments* **89**, 10.1063/1.5010282 (2018).
- [28] A. Gali, Ab initio theory of the nitrogen-vacancy center in diamond, *Nanophotonics* , 1 (2019).
- [29] A. Dréau, M. Lesik, L. Rondin, P. Spinicelli, O. Arcizet, J. F. Roch, and V. Jacques, Avoiding power broadening in optically detected magnetic resonance of single NV defects for enhanced dc magnetic field sensitivity, *Physical Review B - Condensed Matter and Materials Physics* **84**, 1 (2011).
- [30] S. Steinert, F. Ziem, L. T. Hall, A. Zappe, M. Schweikert, N. Götz, A. Aird, G. Balasubramanian, L. Hollenberg, and J. Wrachtrup, Magnetic spin imaging under ambient conditions with sub-cellular resolution, *Nature Communications* **4**, 10.1038/ncomms2588 (2013).
- [31] K. Sasaki, Y. Monnai, S. Saijo, R. Fujita, H. Watanabe, J. Ishi-Hayase, K. M. Itoh, and E. Abe, Broadband, large-area microwave antenna for optically detected magnetic resonance of nitrogen-vacancy centers in diamond, *Review of Scientific Instruments* **87**, 10.1063/1.4952418 (2016).
- [32] M. W. Doherty, F. Dolde, H. Fedder, F. Jelezko, J. Wrachtrup, N. B. Manson, and L. C. Hollenberg, Theory of the ground-state spin of the NV - center in diamond, *Physical Review B - Condensed Matter and Materials Physics* **85**, 1 (2012).
- [33] I. Fescenko, A. Laraoui, J. Smits, N. Mosavian, P. Kehayias, J. Seto, L. Bougas, A. Jarmola, and V. M. Acosta, Diamond Magnetic Microscopy of Malarial Hemozoin Nanocrystals, *Physical Review Applied* **11**, 1 (2019).